



Published in final edited form as:

Nat Med. 2004 April ; 10(4): 422–428.

Noninvasive electrocardiographic imaging for cardiac electrophysiology and arrhythmia

Charulatha Ramanathan¹, Raja N Ghanem¹, Ping Jia¹, Kyungmoo Ryu¹, and Yoram Rudy^{1,2}

*1*Cardiac Bioelectricity Research and Training Center, and Department of Biomedical Engineering, Case Western Reserve University, Cleveland, Ohio 44106-7207, USA.

*2*Department of Physiology and Biophysics and Department of Medicine, Case Western Reserve University, Cleveland, Ohio 44106-7207, USA.

Abstract

Over 7 million people worldwide die annually from erratic heart rhythms (cardiac arrhythmias), and many more are disabled. Yet there is no imaging modality to identify patients at risk, provide accurate diagnosis and guide therapy. Standard diagnostic techniques such as the electrocardiogram (ECG) provide only low-resolution projections of cardiac electrical activity on the body surface. Here we demonstrate the successful application in humans of a new imaging modality called electrocardiographic imaging (ECGI), which noninvasively images cardiac electrical activity in the heart. In ECGI, a multielectrode vest records 224 body-surface electrocardiograms; electrical potentials, electrograms and isochrones are then reconstructed on the heart's surface using geometrical information from computed tomography (CT) and a mathematical algorithm. We provide examples of ECGI application during atrial and ventricular activation and ventricular repolarization in (i) normal heart (ii) heart with a conduction disorder (right bundle branch block) (iii) focal activation initiated by right or left ventricular pacing, and (iv) atrial flutter.

Disruptions of the regular heart rhythm, called cardiac arrhythmias, constitute a major cause of death and disability among the world's population. Although modern medicine relies heavily on noninvasive imaging modalities such as CT or magnetic resonance imaging to guide therapy, an equivalent modality for imaging cardiac arrhythmias is not yet available. Noninvasive diagnosis of arrhythmias is currently based on the standard 12-lead ECG, which involves measuring electric potentials from very few points on the body surface. Taken far away from the heart, these measurements lack sensitivity (may fail to detect abnormal activity) and specificity (may fail to accurately classify the arrhythmia or determine its location). Here we describe ECGI¹, a new noninvasive imaging modality for cardiac electrophysiology and arrhythmias. This technique images potentials, electrograms and activation sequences (isochrones) on the epicardium, the outer surface of the heart. The ECGI methodology used in the human studies presented here builds on 20 years of development in our laboratory (Fig. 1). Many aspects of the approach were tested and validated experimentally in normal and abnormal canine hearts²⁻⁷. Building on these animal studies, we recently developed ECGI for human application. In this report we describe the first ECGI application in human subjects using our current imaging methodology.

Correspondence should be addressed to Y.R. (yxr@po.cwru.edu).

Note: Supplementary information is available on the Nature Medicine website.

COMPETING INTERESTS STATEMENT

The authors declare competing financial interests (see the *Nature Medicine* website for details).

RESULTS

Subject selection

To demonstrate the imaging capabilities of ECGI for normal and abnormal cardiac excitation, we present images from four human studies: (i) normal activation and repolarization (subject N); (ii) right bundle branch (RBB) block (subject R), a conduction abnormality in which conduction through the right bundle branch of the specialized conduction system is blocked, and the impulse originating in the sinoatrial node is conducted from atria to ventricles through the left bundle branch (LBB) only; (iii) right-ventricular (RV) and left-ventricular (LV) pacing (subject P), an example of the ability of ECGI to image ventricular arrhythmias of focal origin, and to locate arrhythmogenic foci (simulated by pacing sites) or exit sites of reentry pathways during ventricular tachycardia; and (iv) chronic atrial flutter (subject AFL), an example of the ability of ECGI to image atrial arrhythmias.

Normal and RBB-block ventricular activation

We imaged ventricular activation in subjects N and R using body surface potentials (BSPs) and subject-specific torso and ventricular epicardial geometry (Fig. 1). Normal and RBB-block activation are compared in Figure 2. Normal ventricular wall activation progresses from the inner surface (endocardium) to the epicardium⁸. An 'epicardial breakthrough' occurs when the activation front arrives and breaks through the surface, generating a local potential minimum in the epicardial potential map⁹. The timing and locations of these breakthrough events provide key information on ventricular activation. We show a BSP map (BSPM), 35 ms after QRS onset (Fig. 2a, left), and the corresponding epicardial potential map (Fig. 2a, right), reconstructed noninvasively from the BSPM using ECGI. This time point showed all epicardial breakthroughs reconstructed in subject N (Fig. 2a, right, dark blue and yellow). The earliest breakthrough, termed the 'RV breakthrough', occurs at the thinnest part of the RV free-wall. RV breakthrough minimum occurred at 22 ms and intensified at 35 ms (Fig. 2a, right, site 1). Several LV epicardial breakthroughs (sites 2, 3 and 4) were also captured. A minimum at site 2 (anterior view) was consistent with breakthrough of the activation front generated by the left anterior fascicular branch of the LBB^{10,11}. The minimum at site 2 and RV breakthrough at site 1 were also observed during direct mapping in chimpanzee hearts¹². Site 3 is at the LV apex and site 4 is in the posterior paraseptal region. Invasive direct mapping^{8, 10,12} of normal activation has documented the occurrence of epicardial breakthroughs at sites 1, 2 and 3, confirming the noninvasive ECGI reconstructions. Breakthrough at site 4 is not always present; it was observed in three of six normal hearts in the Durrer direct-mapping study⁸. The BSPM (Fig. 2a, left) was smooth (single anterior minimum) and showed no indication of the multiple epicardial breakthrough events (Fig. 2b, right).

For subject R we also show the measured BSPM and noninvasive epicardial potential maps for 35 ms (Fig. 2b, left and right panels). At this time point, the BSPM looked very similar to that of subject N, considering the more superior heart position of subject R. However, the corresponding epicardial potential map was different, with no evidence of RV breakthrough (minimum at location 1 in Fig. 2a; maximum in Fig. 2b). We expected this delay in RV free-wall activation, as RBB was blocked. LBB was intact, and the left fascicular breakthrough seemed to be similar to that observed during normal LV activation (site 2, compare with subject N). Observing the temporal progression of epicardial potential maps, we determined RV epicardial activation onset at 49 ms (Fig. 2b, bottom right, location 1). Thus, RV epicardial activation was delayed by 25–30 ms (RV breakthrough in subject N occurred at 22 ms) and ventricular activation occurred sequentially (LV, then RV), rather than simultaneously as in the normal heart. The impulse was conducted in the LBB, activating the left septum and LV free-wall, but was blocked in the RBB. Activation then spread slowly across the septum to activate the RV free-wall after LV activation had already occurred.

Noninvasively reconstructed electrograms from selected sites in subject N (1, 5, 3 and 4) are shown in Figure 2c (left, red). The noninvasive human electrograms were closely similar to invasively measured chimpanzee electrograms¹²; electrogram locations were chosen to allow comparison. Electrogram 1 is from RV breakthrough region (rS morphology); electrogram 5 is from anterior LV (RS morphology); and electrogram 3 is from anterior LV margin (qRs morphology). Invasive human epicardial mapping studies^{13,14} have reported similar morphologies.

We show a noninvasive isochrone map depicting the sequence of epicardial activation for subject N (Fig. 2c, right). Four sites of early epicardial activation (labeled 1–4) corresponded to the epicardial breakthroughs in Figure 2a (right). These four breakthrough sites have also been mapped directly in isolated normal human hearts⁸. Multiple breakthroughs in region 1 (dark red; parallel to left anterior descending coronary artery) have been detected in high-resolution invasive mapping of the canine heart⁹. The posterobasal LV was the last to activate (dark blue, posterior).

For subject R, we show noninvasive electrograms from the anterior paraseptal region (labeled 1) and posterior LV (labeled 4; Fig. 2d, left, blue). Electrogram 1 shows r'S morphology, compared with rS in subject N. The r-wave typically reflects early septal activation followed by RV free-wall activation in the normal heart. In the RBB-block heart, however, where RV activation is delayed, the r-wave reflects the entire septal activation and is wider (40 ms compared with 20 ms in subject N). The rS downslope was uniform and much sharper in subject N, reflecting local RV epicardial activation, compared with the slower initial downslope in subject R, which reflects remote LV activation. Delayed local RV activation was reflected as a second, steeper phase at ~49 ms (arrow). Electrograms from the posterior LV of the two hearts (site 4) showed different morphologies (qR for subject N and qRS for subject R). Subject R's electrogram had a wide and large-amplitude terminal S-wave after LV activation, reflecting delayed RV activation. These morphological differences between subjects N and R characterize most LV electrograms. Activation times for this location were very similar in subjects N (50 ms) and R (46 ms), supporting the observation that LV activation in subject R was normal.

Epicardial activation in subject R is shown in the isochrone map in Figure 2d (right). The earliest activation sites were along the left paraseptal region, corresponding to the anatomical location of LBB. The latest activation was on the basal RV, in clear contrast to subject N, where latest activation was on the posterobasal LV. The crowded isochrones in this area (anterior view) suggest that the area is activated by slow epicardial conduction from the anterior RV.

The standard ECG for subject R is provided in Supplementary Figure 1 online. ECGI animations of the epicardial potential maps for subjects N and R are shown in Supplementary Movies 1 and 2 online.

Activation during ventricular pacing

Subject P had an implanted biventricular pacing device. We imaged for RV pacing alone (Fig. 3a,b) and LV pacing alone (Fig. 3c,d). The epicardial potential map (40 ms from pacing stimulus) for RV pacing is shown in Figure 3a (two identical maps are shown; left map is translucent, showing the pacing lead determined from CT). The site of earliest activation was characterized by an intense, localized RV apical potential minimum (Fig. 3a, asterisk) that corresponded well with the pacing lead terminal. Similar correspondence was seen in the epicardial isochrone map (Fig. 3b, asterisk), where activation spread from the pacing site superiorly to the rest of the RV and apically to the LV free-wall. The lateral LV was the last to activate (dark blue), in contrast with the posterobasal LV in subject N. Electrograms from three locations (shown on isochrone map) show typical morphologies: Q-wave at the pacing

site; qRS at some distance (superior RV) and R-wave far from the pacing site (LV free-wall). This spatial progression relative to the pacing site was also observed by direct mapping².

Translucent and opaque posterior views of an epicardial potential map (40 ms) for LV pacing are shown in Figure 3c. Again, the pacing site was characterized by an intense minimum (asterisk) that corresponded well with the pacing lead terminal in the lateral-paraseptal LV. The isochrone map also showed earliest activation from the pacing site (Fig. 3d, asterisk). Activation spread to the rest of the LV and RV, with the RV base activating last (dark blue). Representative electrograms (superimposed on isochrone map) showed typical morphologies: Q-wave from the pacing site location; qR a distance away (LV free-wall) and R-wave far from the pacing site (anterior RV). Compared with their actual locations (determined from CT), ECGI located the RV and LV pacing sites to within 7 and 11 mm, respectively.

Ventricular repolarization

As demonstrated in the electrograms (Figs. 2-4), ECGI can reconstruct epicardial T-waves well. We reconstructed ECGI images over the ST-T segment in subjects N, R and P (Fig. 4). Unlike activation, repolarization potential patterns are temporally static. We show an epicardial potential map during peak T-wave from subject N as a representative example of normal repolarization patterns during the entire T-wave (Fig. 4a, left panel). Anterior RV electrograms (location 1) show positive (upright) T-waves, while posterior LV electrograms show negative (inverted) T-waves (location 2; Fig. 4a, right). The difference between the activation and recovery times (indicated by vertical lines in electrograms) is the activation recovery interval (ARI), which reflects the duration of the local epicardial action potential¹⁵. The average ARI over the entire epicardial surface was 241 ms (at a heart rate of 64 beats per minute).

Normal repolarization potential patterns have no direct relationship to depolarization patterns because the T-wave is determined mostly by local intrinsic repolarization properties¹⁶. In contrast, the repolarization sequence follows the activation sequence in regions of slow conduction, because intrinsic differences in repolarization times are negligible compared to those introduced by slow progression of activation¹⁶. Consequently, we expected the repolarization potential patterns in such regions to be very similar to the activation patterns, except with reversed polarity^{16,17}. This was demonstrated in the negative repolarization potential pattern of a posterior RV region of subject R (Fig. 4b, left, right lateral view, green-blue), in contrast to the similar but positive pattern in the same region during late activation (Fig. 4b, right, right lateral view, pink-cream). This correlation between potential patterns during activation and repolarization was not observed in other regions of the heart, where conduction is not slow (Fig. 4b, right and left, anterior views).

This dependence of the repolarization sequence on the activation sequence was also seen in subject P (Fig. 4c). The repolarization and activation potential patterns were similar, but opposite in polarity (compare to Fig. 3), as the repolarization sequence followed the activation sequence. For both RV and LV pacing, the minimum of early activation (Fig. 3a,c, blue) was replaced by a maximum (Fig. 4c, white).

Normal atrial activation and atrial flutter

We reconstructed normal atrial activation in subject R using a recorded P-wave BSP, together with subject-specific atrial geometry. A normal atrial activation sequence is depicted by the reconstructed isochrones of subject R (Fig. 5a). Earliest activation (deep red isochrones) was observed in the right atrium (RA), at the anatomical location of the sinoatrial node where the impulse originated. The impulse propagated to the rest of the RA and left atrium (LA). The LA appendage was the last to activate. These noninvasively imaged isochrones are consistent with those recorded directly from isolated human hearts⁸.

Figure 5b demonstrates the ability of ECGI to image atrial flutter in subject AFL, who was diagnosed with typical atrial flutter (sawtooth waves in ECG at 300 beats per minute, average width of 200 ms; Supplementary Fig. 2 online). We show imaged isochrones for one atrial flutter cycle (Fig. 5b, shaded blue on lead V2). The noninvasive atrial isochrone map (Fig. 5b) captured the reentry circuit that drove the flutter. The anterior view shows the circuit (black arrows), which was confined to the RA. The wavefront propagated up the septum (dashed black arrow) and emerged epicardially at the anterior Bachman bundle (asterisk). From there it propagated down the RA free-wall and divided into two wavefronts. One reentered through the isthmus between the inferior vena cava (IVC) and tricuspid annulus. The other propagated around the IVC (white arrow, inferior IVC view) and ascended the lateral RA (white arrow, right lateral view), where it collided with a leftward front (gray arrows) that emerged from the downward-propagating RA free-wall leg of the reentry circuit (black arrow). This collision occurred at the crista terminalis region, an observation that is consistent with direct mapping studies of typical atrial flutter^{18,19}. The anterior and posterior views show wavefront propagation to the LA (gray arrows), which did not participate in the reentry circuit. The LA appendage was the last to activate.

This description of the reentry circuit and activation pattern, based on noninvasive ECGI images, is consistent with observations from direct mapping of typical atrial flutter using intracardiac catheters¹⁹⁻²¹.

DISCUSSION

Cardiac arrhythmias are a major cause of death, disability and compromised quality of life. A noninvasive imaging modality for cardiac electrophysiology is much needed for (i) screening people with genetic predisposition or altered myocardial substrate (such as post-myocardial infarction) for risk of life-threatening arrhythmias, in order to take prophylactic measures; (ii) specific diagnosis of the arrhythmia mechanism to determine the most suitable intervention; (iii) determination of cardiac location for optimal localized intervention (such as ablation, pacing, targeted drug delivery or targeted gene transfer); (iv) evaluation of efficacy and guidance of therapy over time; and (v) studying the mechanisms and properties of cardiac arrhythmias in humans, where the electrophysiological substrate is quite different from experimental animal models used thus far for this purpose. ECGI combines established technologies (BSPM and CT) in a unique fashion to generate noninvasive images of cardiac electrical activity.

Our results demonstrate the ability of ECGI to image human cardiac electrophysiology noninvasively. We provide images of activation and repolarization during normal excitation, RBB block, ventricular pacing and atrial flutter. The normal data serve as baseline controls for imaging of abnormal atrial and ventricular rhythms. We evaluated ECGI reconstructions for subject N by comparison with published invasive measurements in chimpanzees¹² and humans⁸. In subject R, ECGI captured detailed electrophysiological patterns during activation and repolarization that could not be determined from ECG (Figs. 2b,d and 4b). The ability of ECGI to image activation sequences during RV and LV focal activation is shown in Figure 3. The pacing sites simulate ectopic foci (origins of arrhythmogenic activity) and exit sites of reentry pathways—both possible ablation targets in ventricular tachycardia. ECGI located pacing sites to within 7 mm (RV) and 11 mm (LV). Previous canine studies⁴⁻⁶ demonstrated the ability of ECGI to reconstruct abnormal electrophysiological properties and arrhythmias associated with myocardial infarction. The location and extent of the infarct substrate and identification of its abnormal electrophysiological properties (negative epicardial potentials, Q-wave and fractionated electrograms) could be determined from ECGI images. The demonstrated ability here of ECGI to image human epicardial potentials and electrograms suggests that it could detect and locate arrhythmogenic substrates in patients. ECGI also

reconstructed successfully the activation sequence during reentrant ventricular tachycardia in canine models of infarction^{5,6}. A similar capability in humans was shown here for atrial arrhythmias (Fig. 5), where ECGI imaged the reentry circuit responsible for atrial flutter. As observed in direct mapping of typical atrial flutter²⁰, the circuit was located entirely in the RA, with the isthmus between the IVC and tricuspid annulus being the point of reentry (consistent with it being a target for atrial flutter ablation therapy to terminate typical atrial flutter). We also imaged areas of slow conduction (crowding isochrones), wavefront collision at the crista terminalis, and LA activation driven by the RA-reentry circuit.

ECGI could image repolarization abnormalities and regions of increased repolarization dispersion from noninvasively determined ARIs in canine hearts⁷. Such regions provide the substrate for many hereditary and acquired potentially fatal arrhythmias²². The demonstrated ability to determine ARIs in humans noninvasively (Fig. 4a) could open the possibility of obtaining such images in patients, thereby providing information for risk stratification and for guidance and evaluation of therapeutic intervention (such as whether repolarization dispersion is diminished by antiarrhythmic drug therapy).

We demonstrate here the application of ECGI, using examples of imaging normal and abnormal cardiac activity. A detailed mechanistic description of each of the four subject categories (represented here by single examples) will require a systematic application of ECGI in larger groups of subjects.

The ECGI application presented here provides electrophysiological information about the heart surface; it does not directly reconstruct intramural information in the three-dimensional ventricular myocardium. In contrast to BSPMs, however, epicardial potentials provide high-resolution reflection of underlying intramural activity^{9,12}. In canine hearts, ECGI can estimate the intramural depth of pacing sites (simulating intramural ectopic foci)³. In an infarcted canine heart, ECGI provides information, noninvasively, on intramural components of reentry during ventricular tachycardia⁶. More than a third of clinical ventricular tachycardia cases involve the subepicardium, an observation that led to the development of transthoracic epicardial ablation to treat ventricular tachycardia²³. ECGI could be used to guide such interventions and evaluate their outcome in noninvasive follow-up examinations. Intramural depth has less of a role during activation and arrhythmia in the thin atria. That said, ECGI might have limited success in defining components of arrhythmia pathways that involve small volumes of tissue (such as microreentry).

Finally, the need to use CT limits the clinical application of ECGI during intervention in cardiology electrophysiology laboratories, where CT is not available. We recently developed a method for estimating the epicardial surface geometry from biplane X-ray images that can be acquired routinely in the electrophysiology laboratory²⁴.

METHODS

ECGI

We have two requirements for ECGI: (i) electrocardiographic unipolar potentials measured over the entire body surface (BSPs) and (ii) the heart-torso geometrical relationship. A 224-electrode vest strapped to the subject's torso and connected to a multichannel mapping system measured BSP (Fig. 1a). The subject then underwent a thoracic CT scan (Fig. 1a). The CT images (Fig. 1b) provided epicardial surface geometry and vest-electrode positions. The potential and geometry data were then processed through CADIS, the ECGI software package. Details of signal acquisition hardware and software are given below. All protocols were approved by the Institutional Review Board at University Hospitals of Cleveland.

ECGI hardware

There are three main hardware components: a multielectrode electrocardiographic vest, a multichannel mapping system for ECG signal acquisition and an anatomical imaging modality to determine heart-torso geometry. Our prototype vest has 224 dry (requiring no gel electrolyte) Ag/AgCl electrodes, arranged in rows and columns on strips with Velcro attachments at the sides to secure the vest to the torso (Fig. 1a). The vest can accommodate a variety of torso shapes and sizes. A custom-built mapping system facilitates simultaneous signal acquisition and amplification from all channels. The attached computer provides the user interface and storage of acquired signals on optical disk.

We used CT to obtain heart-torso geometry. Scans were usually set to an axial resolution between 0.6 and 1 mm. Scans were typically gated at the R-wave of the ECG to obtain diastolic volume (geometry for reconstruction of activation). We also measured systolic volume (gated during the T-wave of the ECG) to obtain suitable geometry for reconstruction during the repolarization phase. The transverse slices (Fig. 1b) were segmented slice by slice to obtain heart geometry (as epicardial contours on each slice) and torso geometry (described by body-surface electrode positions, seen as bright dots on the images). The geometry of the heart and torso surfaces was then assembled in a common *xyz* coordinate system to provide the geometrical heart-torso relationship (Fig. 1c).

ECGI software

The acquired electrocardiographic signals and CT images were processed by the CADIS custom ECGI software (Fig. 1f) developed in the MATLAB computing package. The software has four modules. The preprocessing module preprocesses the acquired electrocardiographic signals by noise filtration, baseline correction, elimination of bad signals (poor contact) and interpolation of missing signals. The geometry module includes image segmentation algorithms for heart and body-surface segmentation (we typically segmented the atria and ventricles separately) and meshing of heart and torso surfaces (we used linear triangular elements). The numerical module includes boundary element algorithms to derive the transfer matrix relating BSP to epicardial potentials, and epicardial potential reconstruction algorithms that use Tikhonov regularization^{25,26} and the generalized minimal residual algorithm²⁷ to compute unipolar epicardial potentials from the transfer matrix and BSP. Details of our mathematical approach to ECGI have been described previously^{1,25-27}. The fourth module is the postprocessing module, which includes tools to analyze reconstructed epicardial data and formats for efficient visualization and analysis. We typically used four modes of display. (i) Epicardial potential maps depict the spatial distributions of potentials on the epicardium. Each map depicts one instant of time; maps are computed at 1-ms intervals during the entire cardiac cycle. (ii) Electrograms depict the variation of potential with respect to time at a single point on the epicardium. Electrograms are computed at many points (typically 400–900 sites) around the epicardium. (iii) Isochrone maps depict the sequence of epicardial activation based on local activation time, taken as the point of maximum negative derivative ($-dV/dt_{\max}$) of the QRS segment in each electrogram (intrinsic deflection)²⁸. (iv) Recovery times are assigned as the point of maximum derivative (dV/dt_{\max}) of the T-wave segment²⁹. ARIs were calculated as the difference between recovery time and activation time.

Human study procedure

Before the study, we obtained informed consent according to institutional review board guidelines. We cleaned the subject's torso with a water-based spray, then sprayed on a saline-based electrolyte to insure good electrical contact. The vest was placed carefully and strapped on the subject's torso to fit snugly and ensure maximum contact. The patient was made to lie in the supine position, and the vest was connected to the mapping system (Fig. 1a). After the BSPs were monitored to ensure proper contact and gain adjustment, we recorded signals over

several heartbeats (sample signals are shown in Fig. 1d). After signal acquisition, the subject underwent thoracic CT scan, which is the last step in the data acquisition procedure. The ventricular pacing for subject P was performed using the Medtronic Insync-ICD-7272; the protocol included RV apical pacing and LV anterior free-wall pacing, both at a rate of 60 beats per minute.

Supplementary Material

Refer to Web version on PubMed Central for supplementary material.

ACKNOWLEDGMENTS

This study was supported by National Institutes of Health/National Heart, Lung and Blood Institute grants R37-HL-33343 and R01-HL-49054 to Y.R. We thank L. Ciambello for technical assistance in CT imaging; J. Haaga for access to CT; J. Sahadevan, A. Markowitz, A. Waldo, N. Varma and P. Dorostkar for their time, expert advice and access to electrophysiology facilities and patients; and E.T. DuPont for assistance in transporting images from the hospital to our computer facility.

References

1. Rudy Y, Burnes JE. Noninvasive electrocardiographic imaging. *Ann. Noninvasive Electrocardiol* 1999;4:340–358.
2. Oster HS, Taccardi B, Lux RL, Ershler PR, Rudy Y. Noninvasive electrocardiographic imaging: reconstruction of epicardial potentials, electrograms, and isochrones and localization of single and multiple electrocardiac events. *Circulation* 1997;96:1012–1024. [PubMed: 9264513]
3. Oster HS, Taccardi B, Lux RL, Ershler PR, Rudy Y. Electrocardiographic imaging: Noninvasive characterization of intramural myocardial activation from inverse-reconstructed epicardial potentials and electrograms. *Circulation* 1998;97:1496–1507. [PubMed: 9576431]
4. Burnes JE, Taccardi B, MacLeod RS, Rudy Y. Noninvasive ECG imaging of electrophysiologically abnormal substrates in infarcted hearts: a model study. *Circulation* 2000;101:533–540. [PubMed: 10662751]
5. Burnes JE, Taccardi B, Rudy Y. A noninvasive imaging modality for cardiac arrhythmias. *Circulation* 2000;102:2152–2158. [PubMed: 11044435]
6. Burnes JE, Taccardi B, Ershler PR, Rudy Y. Noninvasive electrocardiographic imaging of substrate and intramural ventricular tachycardia in infarcted hearts. *J. Am. Coll. Cardiol* 2001;38:2071–2078. [PubMed: 11738317]
7. Ghanem RN, Burnes JE, Waldo AL, Rudy Y. Imaging dispersion of myocardial repolarization, II: noninvasive reconstruction of epicardial measures. *Circulation* 2001;104:1306–1312. [PubMed: 11551884]
8. Durrer D, et al. Total excitation of the isolated human heart. *Circulation* 1970;41:899–912. [PubMed: 5482907]
9. Arisi G, Macchi E, Baruffi S, Spaggiari S, Taccardi B. Potential fields on the ventricular surface of the exposed dog heart during normal excitation. *Circ. Res* 1983;52:706–715. [PubMed: 6861288]
10. Wyndham CR, et al. Epicardial activation of the intact human heart without conduction defect. *Circulation* 1979;59:161–168. [PubMed: 758108]
11. Kupersmith J. Electrophysiologic mapping during open heart surgery. *Prog. Cardiovasc. Dis* 1976;XIX:167–202. [PubMed: 790461]
12. Spach MS, Barr RC, Lanning CF, Tucek PC. Origin of body surface QRS and T wave potentials from epicardial potential distributions in the intact chimpanzee. *Circulation* 1977;55:268–268. [PubMed: 832342]
13. Jouve A, et al. Epicardial leads in man. *Am. Heart J* 1959;59:856–868. [PubMed: 14407996]
14. Roos JP, van Dam RT, Durrer D. Epicardial and intramural excitation of normal heart in six patients 50 years of age and older. *Br. Heart J* 1968;30:630–637. [PubMed: 5676931]
15. Lux RL, Green LS, MacLeod RS, Taccardi B. Assessment of spatial and temporal characteristics of ventricular repolarization. *J. Electrocardiol* 1994;27:100–105. [PubMed: 7884342]

16. Gima K, Rudy Y. Ionic current basis of electrocardiographic waveforms: a model study. *Circ. Res* 2002;90:889–896. [PubMed: 11988490]
17. Liebman J, Rudy Y, Diaz P, Thomas CW, Plonsey R. The spectrum of right bundle branch block as manifested in electrocardiographic body surface potential maps. *J. Electrocardiol* 1984;17:329–346. [PubMed: 6502050]
18. Matsuo K, Uno K, Khrestian CM, Waldo AL. Conduction left-to-right and right-to-left across the crista terminalis. *Am. J. Physiol. Heart Circ. Physiol* 2001;280:H1683–H1691. [PubMed: 11247780]
19. Yamabe H, et al. Conduction properties of the crista terminalis and its influence on the right atrial activation sequence in patients with typical atrial flutter. *J. Pacing Clin. Electrophysiol* 2002;25:132–141.
20. Daoud EG, Morady F. Pathophysiology of atrial flutter. *Ann. Rev. Med* 1998;49:77–83. [PubMed: 9509250]
21. Rodriguez L-M, Timmermans C, Nabar A, Hofstra L, Wellens HJJ. Biatrial activation in isthmus-dependent atrial flutter. *Circulation* 2001;104:2545–2550. [PubMed: 11714648]
22. Janse MJ, Wit AL. Electrophysiological mechanisms of ventricular arrhythmias resulting from myocardial ischemia and infarction. *Physiol. Rev* 1989;69:1049–1169. [PubMed: 2678165]
23. Sosa E, Scanavacca M, D'Avila A. Endocardial and epicardial ablation guided by nonsurgical transthoracic epicardial mapping to treat recurrent ventricular tachycardia. *J. Cardiovasc. Electrophysiol* 1998;9:229–239. [PubMed: 9580377]
24. Ghanem RN, Ramanathan C, Jia P, Rudy Y. Heart-surface reconstruction and ECG electrodes localization using fluoroscopy, epipolar geometry and stereovision: application to noninvasive imaging of cardiac electrical activity. *IEEE Trans. Med. Imaging* 2003;22:1307–1318. [PubMed: 14552584]
25. Tikhonov, AN.; Arsenin, VY. *Solutions of Ill-Posed Problems*. V.H. Winston & Sons; Washington DC: 1977. The regularization method; p. 45-94.
26. Rudy Y, Oster HS. The electrocardiographic inverse problem. *Crit. Rev. Biomed. Eng* 1992;20:25–45. [PubMed: 1424685]
27. Ramanathan C, Jia P, Ghanem RN, Calvetti D, Rudy Y. Noninvasive electrocardiographic imaging (ECGI): application of the generalized minimal residual method (GMRes). *Ann. Biomed. Eng* 2003;31:981–994. [PubMed: 12918913]
28. Biermann, M., et al. The interpretation of cardiac electrograms. In: Shenasa, M.; Borggrefe, M.; Breithardt, G., editors. *Cardiac Mapping*. Futura Publishing; Mount Kisco, New York: 2003. p. 15-39.
29. Haws CW, Lux RL. Correlation between in vivo transmembrane action potential durations and activation-recovery intervals from electrograms. Effects of interventions that alter repolarization time. *Circulation* 1990;81:281–288. [PubMed: 2297832]

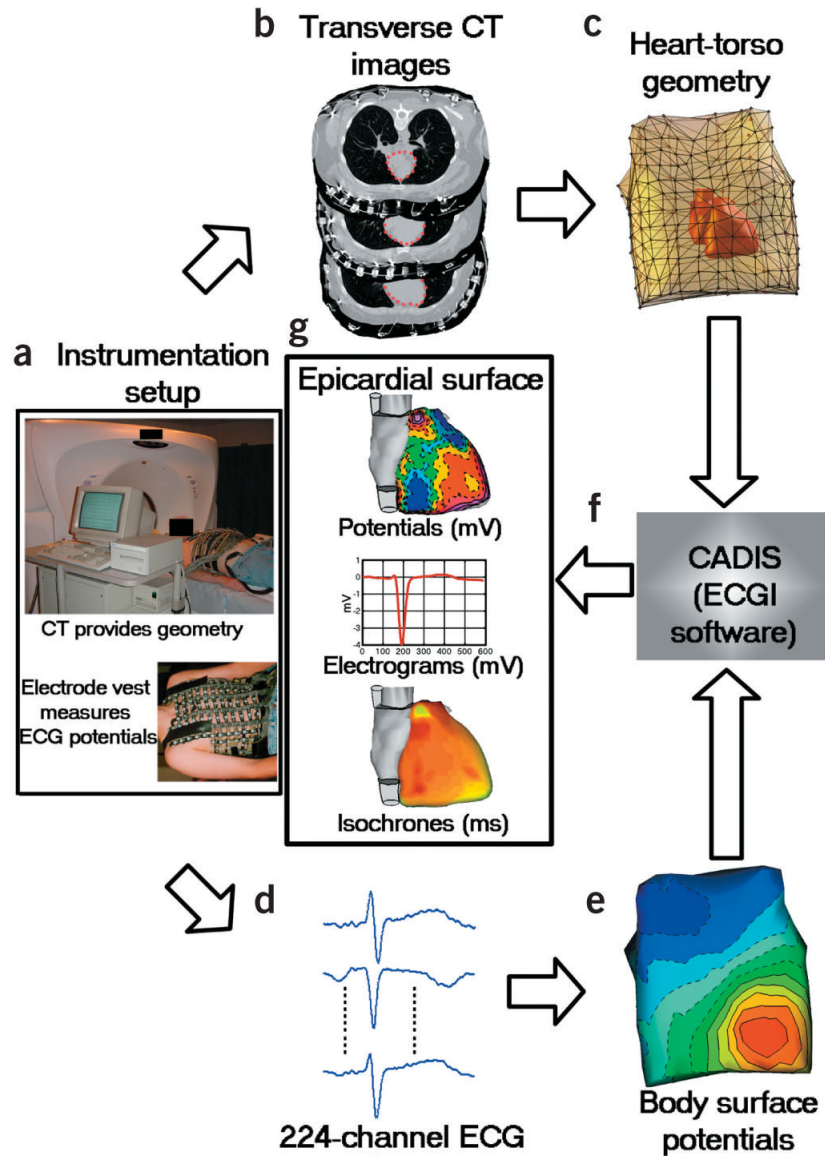


Figure 1. Block diagram of the ECGI procedure. (a) Photographs of instrumentation setup. (b) CT transverse slices showing heart contours (red) and body-surface electrodes (shiny dots). (c) Meshed heart-torso geometry. (d) Sample ECG signals obtained from mapping system. (e) Spatial representation of BSPM. (f) ECGI software package (CADIS). (g) Examples of noninvasive ECGI images, including epicardial potentials, electrograms and isochrones.

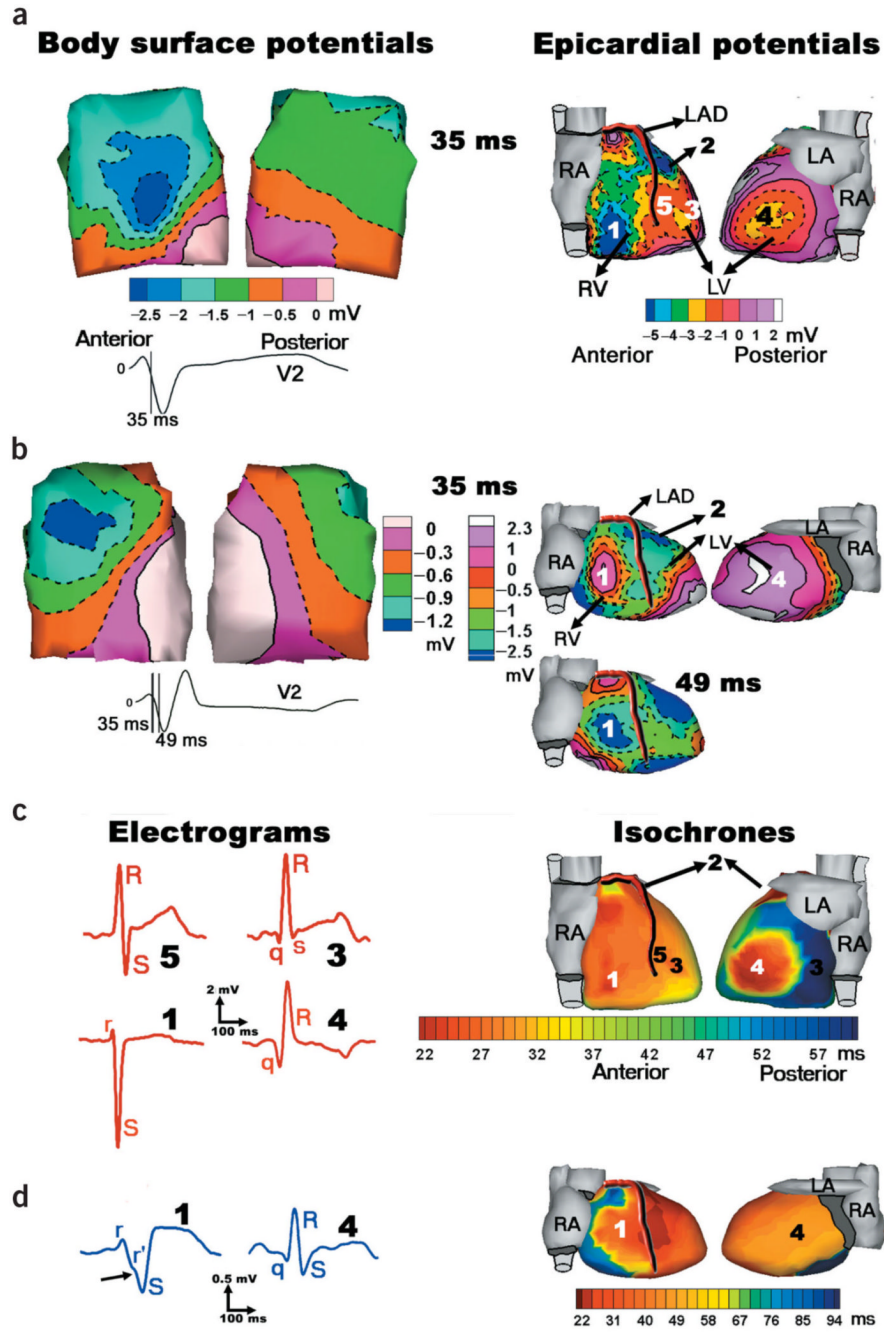


Figure 2. Ventricular activation of subjects N and R. **(a)** Left, anterior and posterior views of BSPM for subject N, 35 ms after QRS onset. Lead V2 of standard ECG is shown for timing purposes. Right, noninvasive epicardial potential map reconstructed from BSPM at left. LAD, left anterior descending coronary artery; LA, left atrium; RA, right atrium. **(b)** Left, BSPM for subject R at 35 ms. Top right, noninvasive epicardial potential map reconstructed from BSPM at left. Bottom right, later noninvasive epicardial potential map (49 ms) showing delayed RV breakthrough (location 1). **(c)** Left, epicardial electrograms for subject N, from locations 1, 5, 3 and 4 (shown in **a**, right). Right, epicardial isochrones. 1, 2, 3 and 4 indicate locations of

early epicardial activation (breakthrough sites). **(d)** Left, electrograms for subject R, from locations 1 and 4 (shown in **b**, top right). Right, epicardial isochrone map.

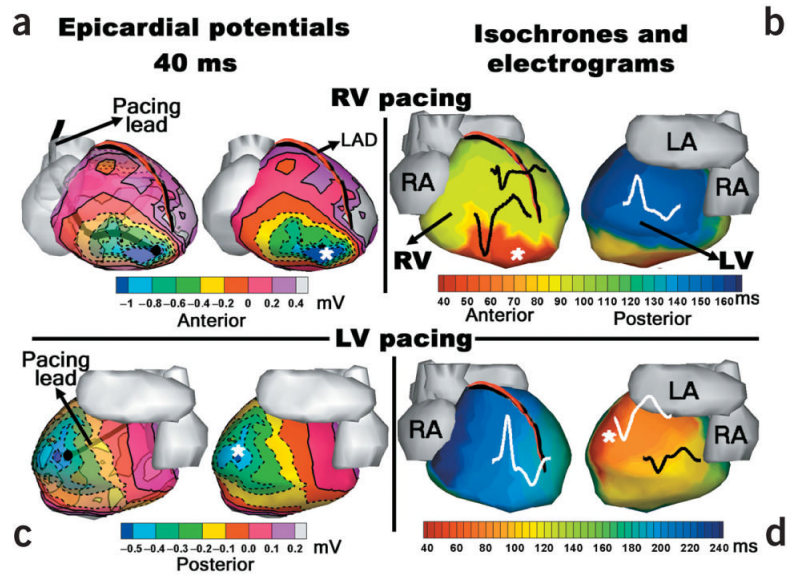


Figure 3. Ventricular activation in subject P during RV (top) and LV (bottom) pacing. **(a)** Anterior views of epicardial potential map during RV pacing. Left, translucent view showing pacing lead. Right, opaque view showing minimum at pacing site location (*). Anterior view is tilted 10° to show pacing site location on inferior RV apex. **(b)** Anterior and posterior views of epicardial isochrone map for RV pacing. Electrograms from three locations are shown at their respective spatial locations. **(c)** Posterior views of epicardial potential map during LV pacing (same format as in **a**). **(d)** Epicardial isochrone map with electrograms for LV pacing (same format as in **b**). LAD, left anterior descending coronary artery; LA, left atrium; RA, right atrium.

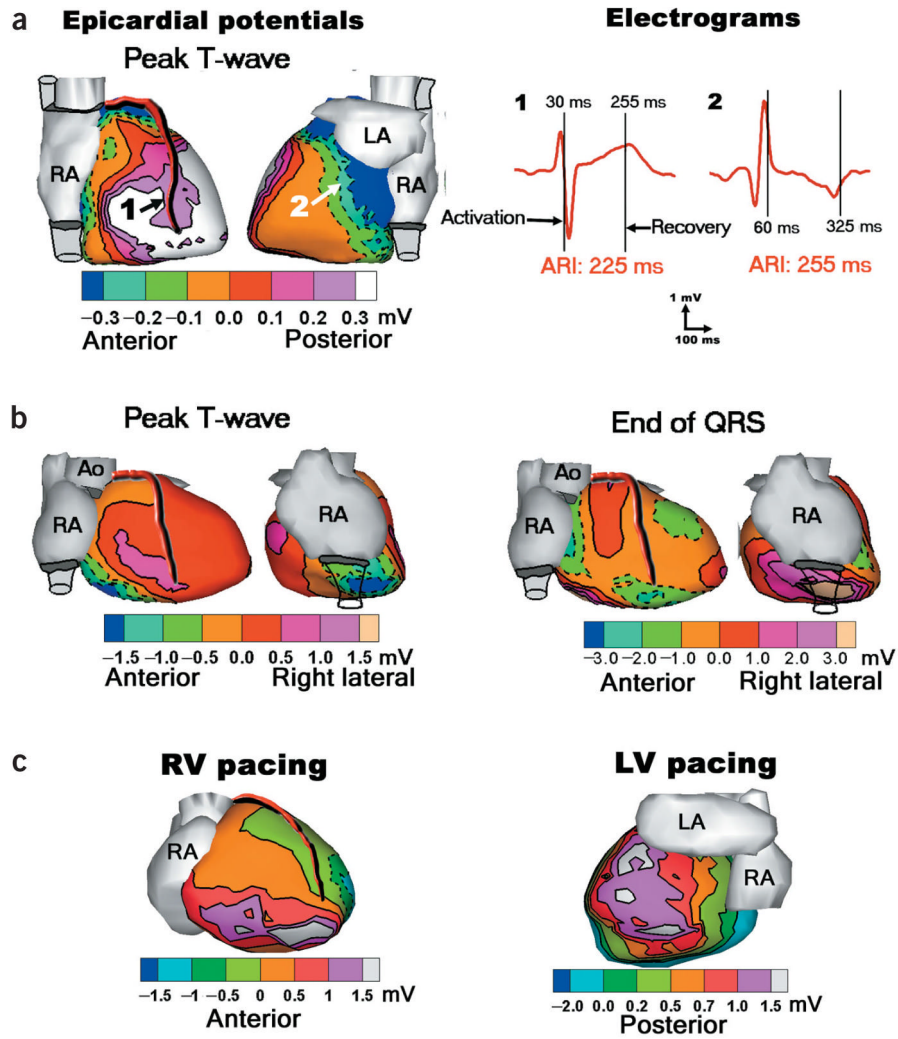


Figure 4. Ventricular repolarization in subjects N, R and P. (a) Left, anterior and posterior views of epicardial potential maps during peak T-wave in subject N. Right, electrograms from locations 1 and 2 (marked in a). Vertical lines mark local activation and recovery times relative to QRS onset. ARI, local activation recovery interval (difference between activation and recovery times). (b) Anterior and right lateral views of epicardial potential maps during peak T-wave (left) and end of QRS (right) in subject R. (c) Left, anterior view of epicardial potential map during peak T-wave for RV pacing in subject P. Right, posterior view of epicardial potential map during peak T-wave for LV pacing. Ao, aorta; LA, left atrium; RA, right atrium.

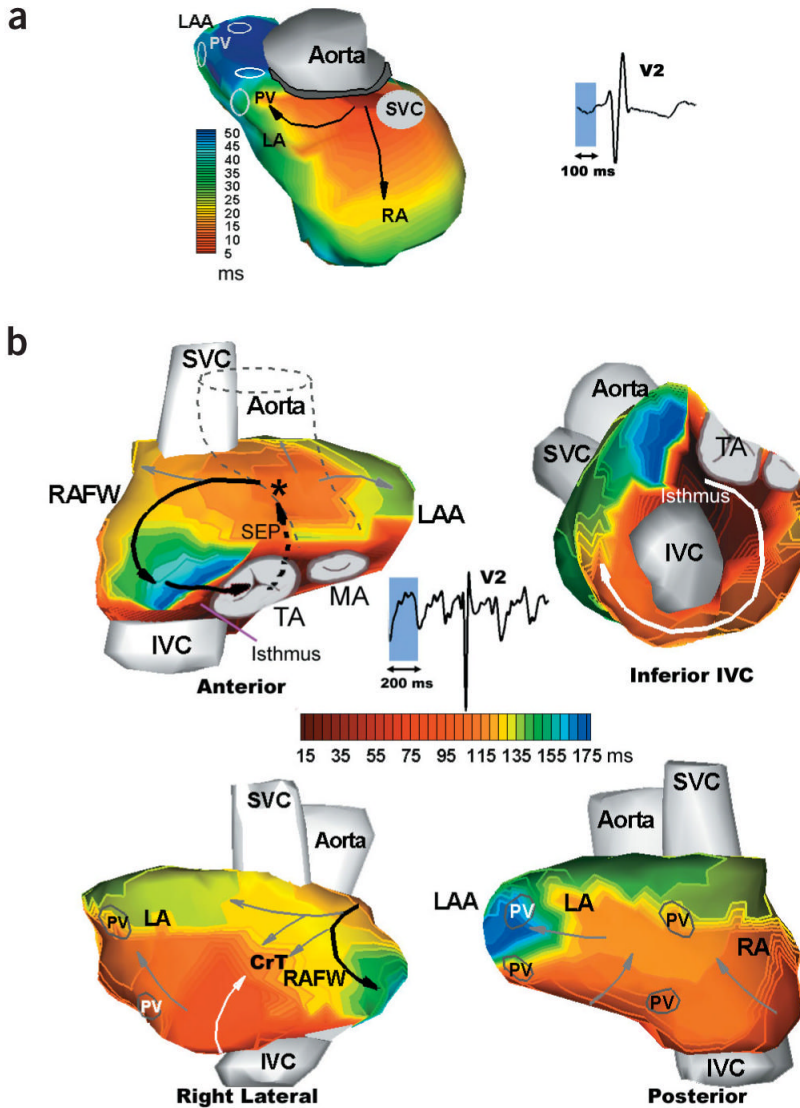


Figure 5. Atrial activation. (a) Normal isochrones for subject R. Left, superior-posterior view. Right, lead V2 of ECG, with P-wave shaded in light blue. (b) Isochrones during atrial flutter in subject AFL. Four views are shown. ECG lead V2 is shown, with imaged flutter cycle shaded blue. Black arrows in anterior view indicate the reentrant circuit beginning from isthmus, entering septum, emerging from Bachman bundle and propagating down right atrial free-wall (RAFW) to reenter isthmus again (a segment of the circuit is also indicated in right lateral view by black arrow). Solid arrows indicate epicardial activation; dashed arrow indicates septal activation. * indicates breakthrough at Bachman bundle. White arrows indicate wavefront propagation around IVC (inferior IVC view) and up RAFW (right lateral view). Activation of LA is shown by gray arrows in anterior and posterior views. LAA, left atrial appendage; SVC, superior vena cava; TA, tricuspid annulus; MA, mitral annulus; PV, pulmonary vein; SEP, septum; CrT, crista terminalis.